Topology optimization and 3D-printing of multimaterial magnetic actuators and displays

Subramanian Sundaram, Mélina Skouras, David S Kim, Louise van den Heuvel, Wojciech Matusik

▶ **To cite this version:**

HAL Id: hal-02397188

https://inria.hal.science/hal-02397188

Submitted on 6 Dec 2019

Topology optimization and 3D-printing of multimaterial magnetic actuators and displays

Subramanian Sundaram,[1,2,⋆] Melina Skouras,[1,3] David S. Kim,[1]
Louise van den Heuvel,[1] Wojciech Matusik [1,2]

[1]Computer Science and Artificial Intelligence Laboratory
Massachusetts Institute of Technology, Cambridge, MA 02139, USA
[2]Electrical Engineering and Computer Science Department
Massachusetts Institute of Technology, Cambridge, MA 02139, USA
[3]Univ. Grenoble Alpes, Inria, LJK, 38000 Grenoble, France
⋆e-mail: subras@csail.mit.edu

Contemporary actuation systems are increasingly required to perform multiple tightly-coupled functions analogous to their natural counterparts; e.g., the ability to control displacements and high-resolution appearance simultaneously is required for mimicking the camouflage seen in cuttlefish. Optimizing and fabricating integrated actuation systems is challenging due to the combined complexity of generating high-dimensional designs, and developing multifunctional materials and their associated fabrication processes. Here we present a complete toolkit consisting of multiobjective topology optimization (for design synthesis) and multimaterial drop-on-demand 3D-printing for fabricating complex actuators ($> 10^6$ design dimensions). The actuators consist of soft hinges and rigid plates made of acrylate polymers and a magnetic nanoparticle/polymer composite (MPC) that responds to a magnetic field. The multi-objective topology optimizer assigns materials for individual voxels (vol-

1

ume elements) while simultaneously optimizing for physical deflection and high-resolution visual properties. Our work demonstrates that unifying a topology optimization-based design strategy with a multimaterial fabrication process enables the creation of complex actuators and provides a promising route towards automated, goal-driven fabrication.

Introduction

Actuators for modern day robots increasingly need to integrate multiple functions together inside a single package to simultaneously optimize for weight, power efficiency, topology, size and other performance metrics. This idea is central to proposals that advocate a tight integration of sensing, actuation, and computation inside robotic materials (*1*), where the distinction between materials and machines are blurred (*2*). This new paradigm requires robot parts to be designed for multiple functions and optimized for multiple objectives as seen in natural organisms. The challenge in reproducing these bio-mimetic multifunctional systems is explicitly evident in the design of actuation systems. A classic example is the actuation system in cuttlefish that controls both the physical deflections (papillae in the skin) and the high-resolution appearance (multilayer metachrosis). Controlling these two abilities (physical deformation and appearance control) simultaneously is essential for effective camouflage (*3–5*). Reproducing such seamlessly integrated actuation systems that optimize for multiple objectives is challenging due to the complexity that exists in: (i) designing in a high-dimensional design space (with many design variables) while optimizing for multiple objectives, and (ii) fabricating these designs with new materials and in free-form geometries.

Many examples of contemporary actuation systems of high-complexity consist of microscale actuators tiled into regular arrays. The Digital Micromirror Device (DMD) (*6*) with millions of identical actuators (*7*) and the "Millipede", a high-density data storage system consisting

2

of microelectromechanical system (MEMS) cantilevers (1024-element actuator array) (*8*) are two impressive examples. However, optimizing these actuation systems (with identical actuators) for power consumption, low-footprint and process reliability still requires a significant amount of time. It is noteworthy that a similar system with non-uniform actuator arrays would present a bigger design complexity. On the other hand, designs pervasive in natural organisms present several examples of actuator collections with high design complexity that are optimized through evolution. Some examples are: (i) denticle patterns attached to the epidermis and dermis of sharks that together control the hydrodynamic drag (*9, 10*), (ii) cilia in comb jellies (*Ctenophora*) that synchronously beat for efficient propulsion (*11*), and (iii) coordinated legs in centipedes and other arthropods (*12–14*).

As complexity of actuator designs increases, it is challenging to design such systems by hand. Topology optimization techniques that automatically generate optimized material layouts within a given design space offer a promising alternative (*15*). In this context, gradient-based methods, initially proposed for structural design optimization (*16*), appear to be very effective for a wide range of applications, ranging from the design of photonic crystal structures (*17*), to passive (*18, 19*) and active (*20*) compliant mechanisms and elastic meta-materials (*21*). However, while such approaches are well suited to obtain smooth layouts as is often desired in the case of elastic structures, these are not appropriate for designs which require dithered material distributions that satisfy high-level functional goals. Briefly, gradient-based optimization methods introduce challenges in this context. When working directly with dithered material distributions, the risk of being trapped in a local minimum is high, whereas using indirect representations may change the non-linearity of the problem itself or make it challenging to incorporate fabrication-related phenomena. Stochastic methods such as evolutionary algorithms, by contrast, are useful when seeking to explore large solution spaces and to promote indirect solutions involving complex objectives such as locomotion (*22, 23*). In our work, we turn toward

3

a simulated-annealing strategy, which has been successfully applied in the context of topology optimization to design truss structures (*24, 25*) and whose stochastic nature is particularly appealing for optimizing visual properties (*26*). However, while very generic in theory, this approach needs to account for the specifics of the problem to be effective in practice. In our design synthesis task, achieving good optical properties requires working at the resolution of fabrication (i.e., printer resolution), which in turn requires that we take into account phenomena such as droplet spreading. Similarly, the optimization approach needs to consider the role of the materials - e.g., high opacity of one of our inks requires that we use dedicated techniques such as half-toning to widen the range of perceived pixel intensities. In other words, the topology optimization approach has to be fully fabrication-aware. As far as we know, such a high-resolution, multiphysics and fabrication-aware topology optimization framework has never been proposed in the past.

Fabricating the synthesized actuator designs demands a manufacturing process that is capable of handling high-dimensional designs. In parallel, the fabrication method needs to be capable of achieving high spatial resolution. New fabrication methods for multifunctional actuators for camouflage applications is a topic of current interest (*27–29*) but achieving high-resolution appearance properties is a current challenge. We chose an additive manufacturing approach for our actuator fabrication due to rapid progress in 3D-printing that has enabled precision manufacturing (*30, 31*) of complex structures (*32–36*) with diverse materials (*37–42*). Interest in 3D-printed actuators is growing due to their applicability for use in micro/mesoscale robotics (*43–47*). Magnetic actuation in particular has been extensively explored (*48, 49*) for soft matter applications (*50*) due to its favorable scaling, high actuating force density and potential for untethered actuation (*51, 52*).

We postulated that unifying a bio-mimetic evolutionary optimization technique with an automated multimaterial additive manufacturing process would enable the rapid design and fab-

rication of high-dimensional actuators. Additionally, this would eventually enable the fully-automated fabrication of high-dimensional designs, which has been a long-term goal in robotics (*53*). Note that we refer explicitly to the dimensionality of the design space (or number of design variables) throughout this work. Here, we demonstrate the first topology-optimized multimaterial actuator with more that 10^6 design dimensions that is optimized simultaneously for displacement and high-resolution appearance constraints. These actuators are fabricated using a custom drop-on-demand 3D printing process, allowing us to optimize the entire fabrication pipeline and perform fabrication-aware optimization. The specific actuator design we demonstrate is a planar, rigid structure consisting of, for instance, $186 \times 186 \times 160$ cells that can each be filled with either a transparent rigid polymer or a dark magnetically-responsive polymer. Our topology optimizer controls the placement of the two materials based on their material properties to optimize for the target objectives. In our demonstrations, the two individual objectives are input images (appearance objective) and target tilting angles (displacement objective). This topology-optimized rigid plate actuator is supported on the sides by two torsional elastic hinges. The optimized structure is then fabricated by our custom printing process.

Results

We combine a custom multimaterial drop-on-demand 3D-printing process with multi-objective topology optimization to fabricate high-dimensional actuator designs generated from functional objectives, as outlined in Fig. 1. Briefly, we first create a set of UV curable inks with varied properties (optical, magnetic and mechanical properties) and characterize samples printed with these inks to generate a property library. The characterized material properties are then used in conjunction with functional objectives (the appearance and the displacement field in this case) as inputs to the voxel-level topology optimizer that generates the material composition. The generated output is used by our custom-built multimaterial 3D-printer to fabricate the optimized
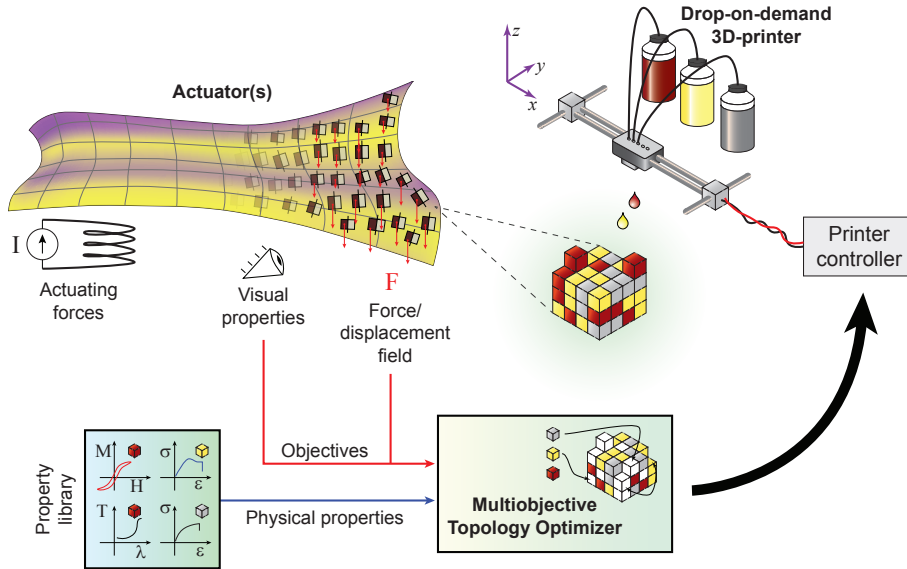
Figure 1: **Overview of the specification-driven 3D-printing process.** The structure of individual actuators (or the arrangement of multiple actuators) is optimized using a multi-objective topology optimization process. Note that in general, the final optimized structure can be of any arbitrary shape as shown. The optimization uses the bulk physical properties of the individual materials and the functional objectives as inputs. The generated optimized voxel-based representation of the structure is used by the printer to fabricate the optimized structure using a drop-on-demand inkjet printing process. This allows high-dimensional designs to be automatically generated and fabricated with minimal human intervention. In this work, a rigid acrylate polymer (RIG), an elastic acrylate polymer (ELA) and a magnetic nanoparticle (Fe_3O_4)/polymer composite (MPC) are the main materials used. The contrast in the optical, mechanical and magnetic properties is used to simultaneously optimize the visual appearance and the actuating forces while generating the voxel-level design.

actuator design. It is noteworthy that the generated actuator design may occupy any arbitrary shape as shown in Fig. 1. Here we constrain the actuator to fill a predefined grid (plate); the internal structure of the two materials are irregular and non-planar.

Drop-on-demand 3D-printing and material properties

Drop-on-demand 3D-printing is an additive manufacturing process that provides the ability to print diverse materials simultaneously at a uniform resolution. We use a custom built inkjet-based multimaterial 3D-printer with ~ 35 µm lateral resolution (*42, 54*). So far, this process has

been used to print UV curable solid materials, encapsulated liquids, and electrically conducting and semiconducting inks (*36, 42*). This is emerging as a promising technique to achieve printed actuators (*55, 56*). Broadly, the main material limits for the printing process come from the rheological properties of the starting ink (*57*). Typically, inks with viscosity 3 - 15 cP and surface tension 40 mN/m are ideal for our printing process, and the maximum particle size is maintained well below one-tenth the nozzle diameter to prevent clogging ($\ll$ 3 µm) (*42, 54*).

The main materials we use in this work are a rigid acrylic polymer (RIG), an elastic polymer (ELA) and a magnetic nanoparticle/polymer composite (MPC). The starting inks are formulated from acrylate monomers and oligomers along with photoinitiators that absorb at 365 nm (*i*-line), and are optimized for an inkjet printing process. The appropriate inks are deposited by the printhead for each voxel from the generated stack of layered bitmaps containing the material assignments. Subsequently, after deposition of inks in each pass, a UV LED array is used to crosslink the inks using free-radical photopolymerization (see Materials and Methods for more details of the ink formulations and the printing process).

We generated the property library shown in Fig. 2 from thin printed slabs of different materials; the material is indicated as a cube in the bottom right (brown, yellow and gray correspond to MPC, RIG and ELA respectively). The crosslinked magnetic material (MPC) is nearly opaque beyond $\sim$ 100 µm thickness while the rigid polymer (RIG) is nearly transparent as shown in the transmission factor measurements in Fig. 2A and 2B. The magnetic composite, MPC ($\sim$ 12 wt% Fe_3O_4 nanoparticles in the acrylic polymer ink; see Materials and Methods and fig. S1) with a saturation magnetization of $\sim$ 5 emu/g (see Fig. 2C) is used to generate the forces and torques in our actuators. The three materials also have widely varying elastic moduli - ELA (528 kPa), MPC (507 MPa) and RIG (1290 MPa) - averaged from 3 individual samples. Representative stress - strain curves are shown in Fig. 2D, 2E and 2F. ELA and RIG differ in their elastic moduli by over 3 orders of magnitude. This allows us to make soft joints
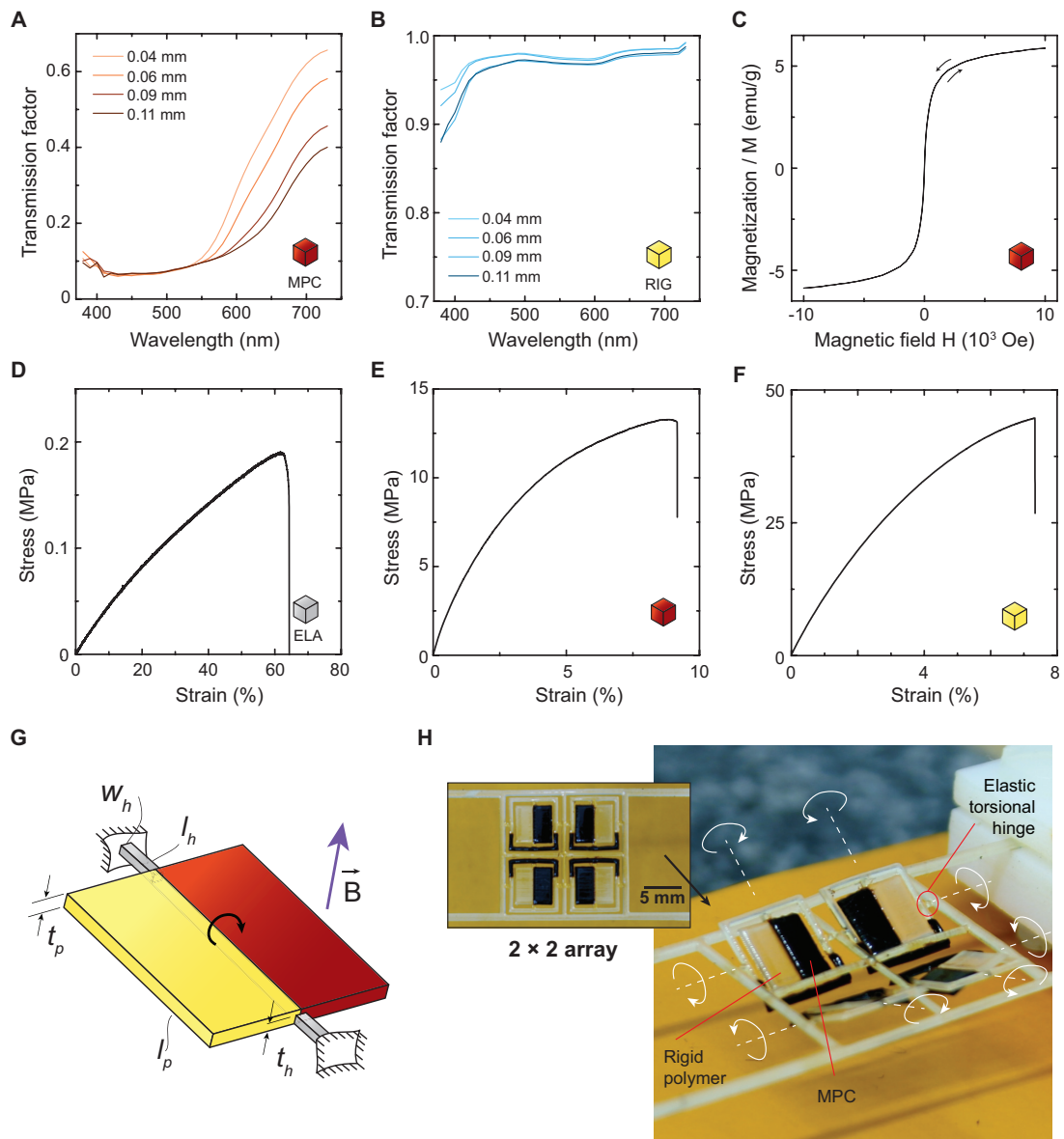
Figure 2: (Caption below)

Figure 2: **Material property library.** **(A)** The transmission through the MPC shown as a function of the wavelength for films of varying thickness, measured using a spectrophotometer. **(B)** The transmission through the clear rigid material shown as a function of wavelength for multiple film thicknesses. **(C)** Magnetization versus applied magnetic field for the MPC measured at room temperature. Magnetic nanoparticles make up ∼12 % of the overall weight of the MPC. Typical mechanical stress-strain curves for the elastic polymer (ELA), MPC and the rigid polymer (RIG) are shown in **(D)**, **(E)** and **(F)** respectively. Elastic moduli of the polymers at linear strains, averaged from three samples each, vary significantly - ELA (528 kPa), MPC (507 MPa) and RIG (1290 MPa). **(G)** The schematic shows the fundamental hinge-based design with panel length l_p, and thickness t_p. In this design, the panel is sectioned into two equal portions of RIG and MPC. The panel is attached to rigid boundaries on two sides with ELA torsional hinges of length l_h, width w_h, and thickness t_h. On the application of a magnetic field, the magnetic portion of the panel generates a torque. This is used as the fundamental block in the manually designed samples. **(H)** Image of a 2×2 array of panels each with two axes of rotation. The dark brown regions of the image show the MPC material, and the translucent portions show the rigid materials. The elastic torsional hinges are nearly identical to the rigid polymer in appearance. On the application of a magnetic field, each panel exhibits a unique combination of two-axis angular rotations. The top view of the flat as-printed sample is shown on the left.

with ELA while making rigid structures with RIG. These measured mechanical properties are used later in our simulations to evaluate mechanical deflections of our designs in response to actuating forces. The contrast in the optical transmission and magnetic properties are used in our actuators designed manually and by the multiobjective topology optimizer.

Multimaterial soft actuators

We first demonstrate the capabilities of our base material set, and fabricate a variety of multi-material actuator arrays designed manually. The fundamental design unit used in our actuator arrays is illustrated in Fig. 2G. In this design, a square panel of size l_p and thickness t_p is partitioned into two equal halves of the RIG and MPC materials. The panel is suspended at the center by two identical elastic torsional hinges (ELA) of length l_h, width w_h and thickness t_h. On the application of a magnetic field, the paramagnetic material in the MPC region of the structure is attracted towards the magnetic field, generating a net torque that is balanced by the torsional

9

springs. Experimental results of the tilting angle are verified by simulations (see "Soft-joint simulation" section in Materials and Methods and fig. S2). These calibration measurements are used to refine the measured mechanical properties of the elastic hinge (ELA). The general design is extended to generate 2-axis torsion in the panel by adding a rotating frame tilting in orthogonal directions. A printed 2×2 array of 2-axis rotating panels is shown in Fig. 2H under an applied magnetic field (design and more images in fig. S3; see "Magnetic Field" section in Materials and Methods for testing setup).

In order to evaluate the performance metrics of these actuators, we use the actuator design shown in Fig. 3A ($l_{p1} \times l_{p2}$ = 8 mm $\times$ 9 mm, t_p = 1 mm, λ = 0.15, W_h = 0.5 mm, l_h = 1 mm and t_h = 0.25 mm). The blocking force generated by these actuators is measured at the edge with the maximum displacement using a polyimide cantilever of calibrated stiffness (k_{cant} = 105.9 $\pm$ 12.0 mN/m; details in Materials and Methods) as a force probe. Figure 3B shows the measured force (calculated from the cantilever displacement) as a function of the distance between the 2" $\times$ 2" $\times$ 0.5" magnet and the sample. The corresponding results obtained from our simulations is shown as a solid curve; solver details are described in "Soft-joint simulation' section of Material and Methods. When the blocking cantilever is removed, the angular deflection of the sample can be measured and is shown in Fig. 3C along with our simulation results. We next estimated the speed at which these actuators can be actuated using an electromagnet. First, we optically tracked the edge of the panel when it was actuated in the small amplitude regime ($< 1°$) as the frequency of the current pulse was varied from 0.01 Hz to 10 Hz. The angular displacement ($\Delta\theta$) is measured for 3 identical devices; one is shown in Fig. 3D. The measured peak displacement amplitude as a function of frequency (Fig. 3E) shows that these actuators exhibit a damped frequency response with a -3 dB actuation bandwidth $\sim$ 0.32 - 0.56 Hz. Note that the damped response is consistent with the measured loss modulus for our elastic material family (fig. S4); the storage modulus is equal to the loss modulus

10
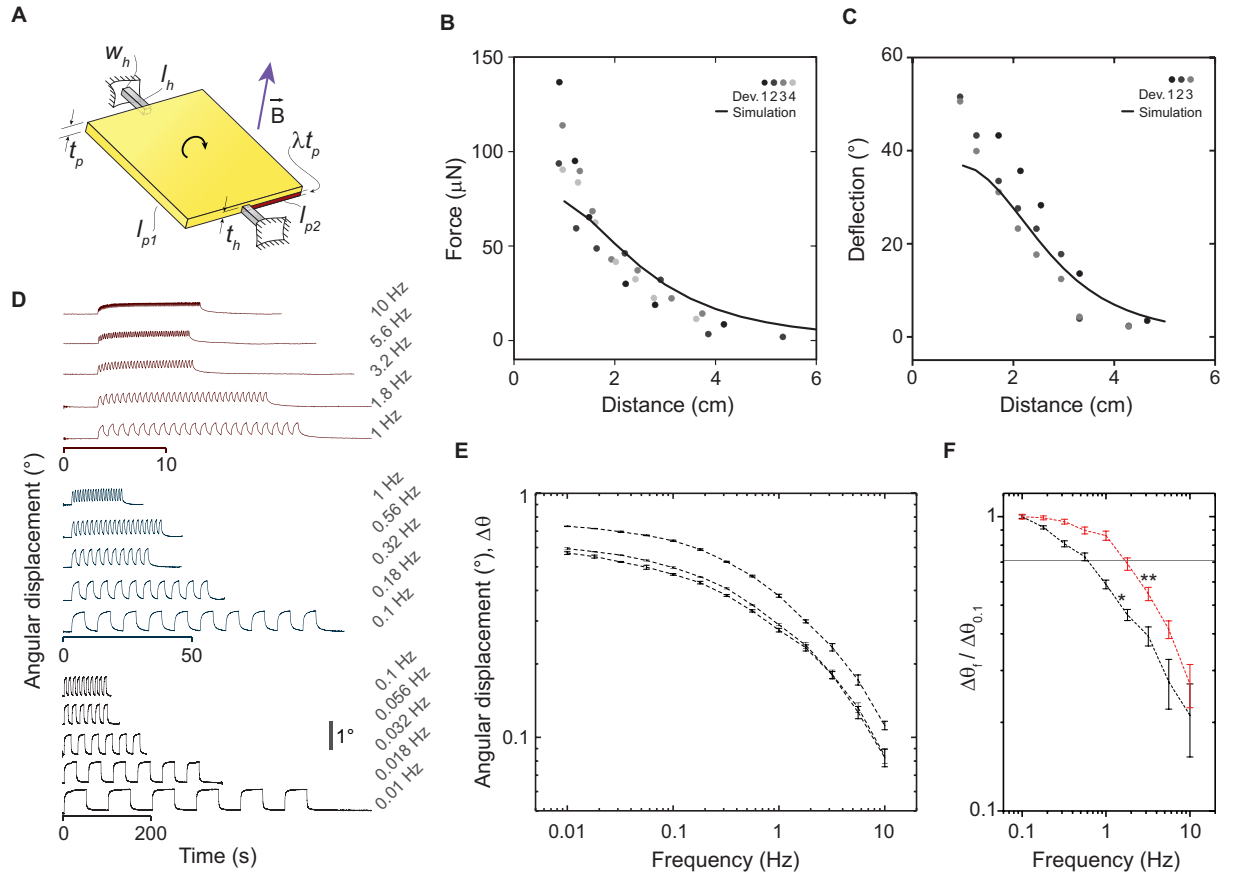
Figure 3: **Actuator characteristics - forces, displacements and actuation bandwidth. (A)** In order to characterize the actuator performance, we use the fundamental design (Fig. 2G) with a small change. Here only a fraction of the panel thickness, t_p, is filled with MPC, denoted by λ. The following results were obtained with a rectangular panel of size $l_{p1} \times l_{p2} = 8$ mm $\times$ 9 mm, thickness $t_p = 1$ mm, $\lambda = 0.15$, and hinges with dimensions $W_h = 0.5$ mm, $l_h = 1$ mm and $t_h = 0.25$ mm. **(B)** Measured blocking forces of 4 identical devices shown as a function of the distance from the 2" $\times$ 2" $\times$ 0.5" magnet along with corresponding simulation results (see magnet, measurement setup and simulation details in Materials and Methods).**(C)** Measured angular deflections of 3 identical devices as a function of distance from the magnet. **(D)** Optically tracked angular displacements as function of time for actuation at frequencies from 0.01 Hz to 10 Hz. **(E)** Angular displacement amplitudes as a function of frequency for three devices. **(F)** The apparent large-amplitude bandwidth depends on the setup of the magnetic field since the force experienced by the actuator itself varies with the displacement. This is highlighted in this plot with two cases - in one case, the force experienced by the actuator increases monotonically with angular displacement ($\star$) and in the other case with a stable angular displacement when the panel aligns with the direction of maximum gradient ($\star\star$). See fig. S5 for corresponding time curves, and details of the setup.

11

measured at 1 Hz actuation at ∼23.7 °C. The bandwidth measurement at large amplitudes is less straightforward since the force experienced by the actuator varies as a function of displacement. To highlight this we consider two cases where the actuators are oriented differently - in one case the force experienced by the actuator increases with increasing displacement (⋆) where as in the other case there is a stable angular position where the actuator panel aligns with the direction of maximum flux density and gradient (⋆⋆). Therefore, the apparent large-amplitude bandwidth can exceed the small-amplitude bandwidth based on the setup of the field as shown in Fig. 3F (see Video S3). The corresponding angular displacements and images are shown in fig. S5. These actuators can be cycled for at least 1000 cycles with no apparent degradation in performance (fig. S6, Video S3).

To highlight the potential of multimaterial actuator arrays in passive display applications, we enhance the fundamental actuator design (Fig. 2G) with two extra materials, as shown in Fig. 4A. Vertical slabs are printed on top of each panel with RIG mixed with a white pigment. The sides of the vertical slabs are textured with cyan-colored polymer such that different images can be displayed by controlling the panel's pitch. The panel array is designed to show the letters "MIT" when actuated by a magnetic field.

To dynamically actuate our printed displays, we utilize an electromagnet powered by a current source to generate a tunable magnetic field. We print an array of 6 elements on a special substrate to produce a mirror-like finish on one side of the print. This substrate is prepared by drop casting and annealing a reactive silver ink on a polyimide sheet (see Materials and Methods). The silver layer peels along with the print as the actuator array is removed from the polyimide film (after printing). The silver regions freely exposed on both sides are then etched. A laser line is projected on to the reflective side of these panels and the angular tilt of the panels is dynamically controlled using the electromagnet using the setup shown in Fig. 4B. The laser line reflected from the mirror array is imaged on a screen; here, the panels are designed to tilt

differently to raster the MIT logo shown in red (Video S1). Schematic of the physical setup is shown in fig. S7. The two images shown in Fig. 4C are photographs of the laser line on the printed actuator array, and the screen when the electromagnet is turned off, and when powered by a 7.5 A current source (magnetic field settings are described in Materials and Methods).

A critical advantage of magnetic actuation is in the potential for untethered actuation, which is useful in conductive or liquid environments where electrically driven actuators need careful electrical isolation. Furthermore, magnetic actuation is also useful for actuation inside the body without requiring any external connections for actuation, i.e., the actuated part does not require a physical connection to a power supply (58). In Fig. 4D-4F, we show untethered actuation
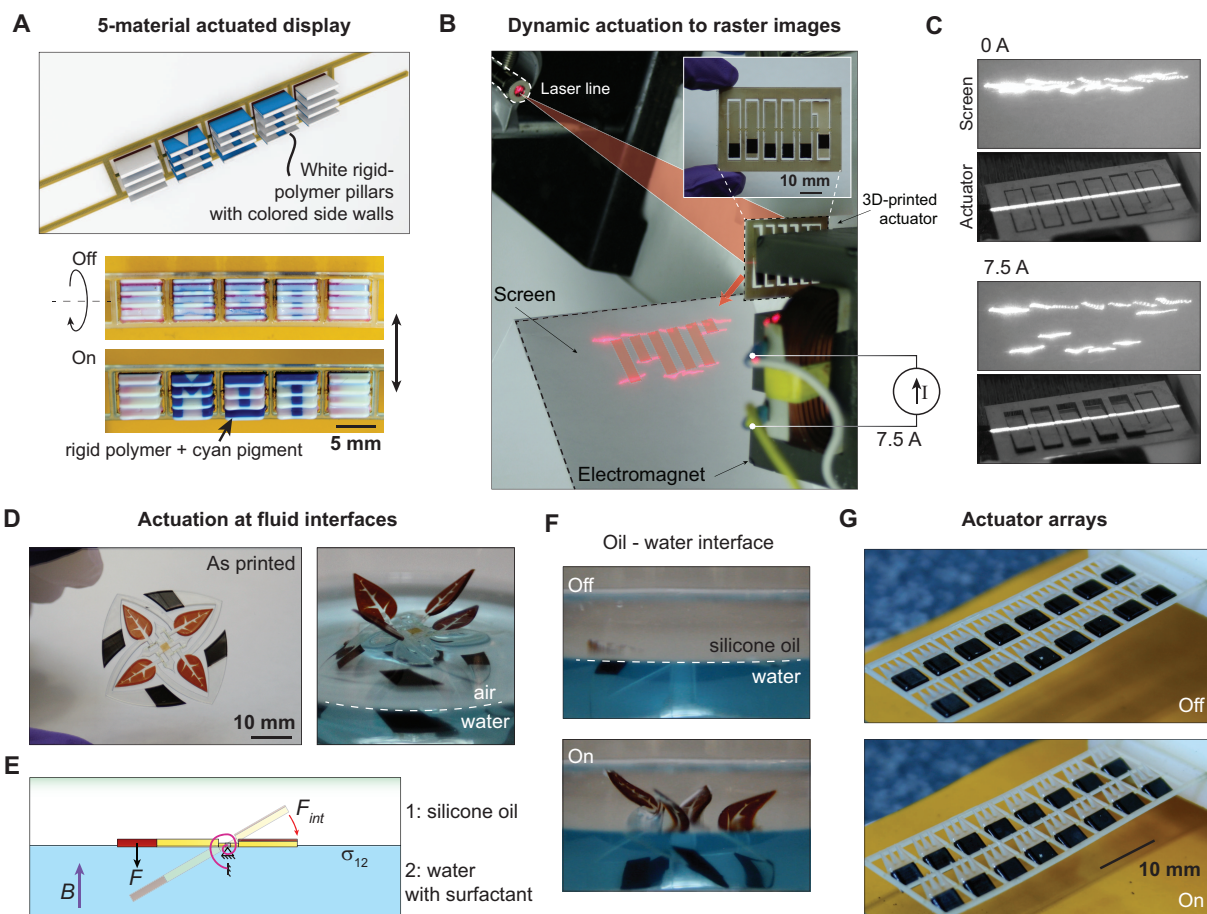

Figure 4: (Caption below)

Figure 4: **Applications of 3D-printed multimaterial soft magnetic actuators. (A)** 5-material actuated display. Each panel consists of the design shown in Fig. 2G on top of which 4 vertical walls of a white rigid polymer are printed. The side walls are patterned based on the image to be displayed. Here the letters "MIT" are chosen to be patterned on the sidewall. An applied magnetic field generates a torque on the panel allowing different sides of the walls to be visible from a fixed viewing angle. **(B)** A 6-element array of mirrors is is mounted next to an electromagnet powered by a current source (0 A - 7.5 A). The torque experienced by each individual panel is controlled by the position of the MPC regions. Different images are rastered on a screen by shining a laser line across the mirror array. Here the panels are designed to raster the MIT logo. See fig. S7 for a schematic of the setup. **(C)** The two sets of images show the still photographs of the screen, and a snapshot of the mirror array with the electromagnet turned off and on (7.5 A). Dynamic actuation using a linear current ramp is shown in Video S1. **(D)** To demonstrate the use of the magnetic actuator arrays in liquid interfaces, we design water lilies that are positioned on water interfaces. The petal patterns are printed using 3 layers of the magnetic ink, and torsional hinges are made from the elastic polymer. (Left) The top view of the as-printed part is shown where the solid dark regions are the actuating regions made with MPC. (Right) When placed on the air-water(with $0.2\ \%$ FC4430, $\sigma = 20.9$ mN/m) interface, the leaves are held flat due to the interfacial tension of water. While it can be deformed by an applied field, as shown, some panels return to their flat position easily when the water is disturbed. **(E)** When tested in conditions with lower interfacial tension $\sigma_{12} = 3.7 \pm 0.78$ mN/m (interface of silicone oil and water with $0.2\ \%$ FC4430), the array can be actuated back and forth reliably (Video S2). The schematic shows the restoring nature of the interfacial tension. **(F)** Experimental results of actuation at the silicone oil-water interface. **(G)** An array of 16 identical actuators with serrated edges is shown with and without an applied magnetic field (design in fig. S9).

in conductive fluid interfaces. The image on the left (Fig. 4D) shows the as-printed sample, containing four individual petals that can be actuated. When the printed device is placed on the air-water (with surfactant, and colored blue) interface, as shown on the right, the petals can be lifted up from the water surface by attracting the magnetic regions (design in fig. S8). However, the larger interfacial tension makes repeatable actuation challenging. Repeated actuation cycles can be performed when the printed sample is placed at the silicone oil - water interface (interfacial tension $\sigma_{12} = \sim 3.7$ mN/m), schematically shown in Fig. 4E. Experimental results are shown in Fig. 4F and Video S2. It is noteworthy that the elastic hinge effectively acts as a rotating joint here. The torsional stiffness is dominated by the interfacial tension experienced

by the petals when leaving the silicone oil-water interface.

It is generally easy to scale the number of elements in these actuator arrays by tiling identical actuators. To demonstrate this, we tile actuator panels with spikes (Fig. 4G; see fig. S9 for design), inspired by the geometry of scales seen on shark skins.

These hand-designed examples highlight the utility of multimaterial additive fabrication in creating magnetic actuators. This fabrication platform uniquely enables the easy integration of multimaterial printing with voxel-level topology optimization required for high resolution optical properties. We now discuss the topology optimization technique and show that this approach makes it feasible to tackle complexity (large number of design variables) in the actuator design pipeline.

Multi-objective topology optimization

We choose an actuator design problem with more than 10^6 cells whose material assignments are computationally generated using topology optimization. Specifically, we fabricate an actuator that deflects and changes its appearance in the presence of a controlled magnetic field. The basic actuator unit is a single panel actuator, supported by two ELA hinges, that is divided into a hexahedral lattice of cells whose individual material assignments are optimized by simulated annealing. This results in actuators that change their appearance to various unrelated images at specific tilt angles (or torques). The multiple objectives here can be considered as a series of image and torque pairs. The general architecture, inspired in part by multilayer tensor displays (*59*), is also indirectly motivated by the multilayer nature of metachrosis used by cuttlefish for camouflage (*4*).

For each panel, our topology optimization component takes as input, n grayscale images $\tilde{I}^i$, $i = 1..n$, represented as arrays of pixel intensities, n target angles for the panels corresponding to the desired tilting angles and n distances d_i corresponding to the distances between the panel
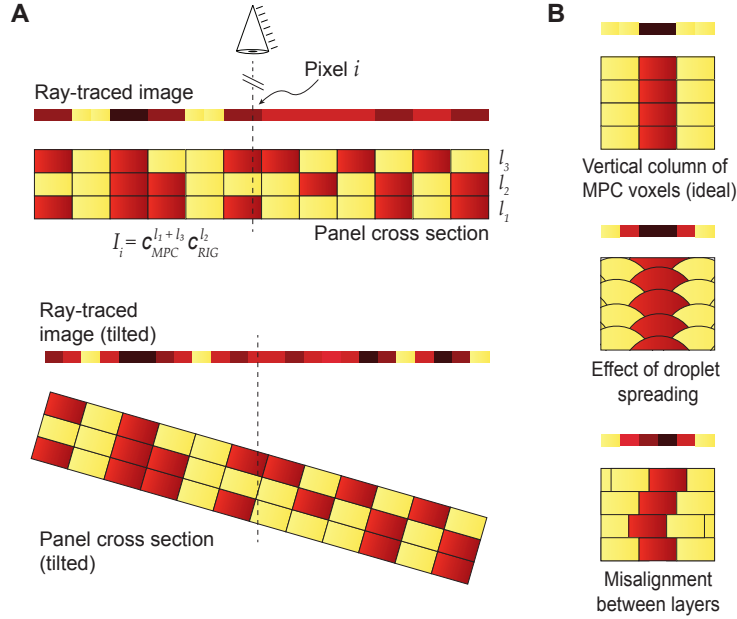
Figure 5: **Panel appearance computation.** (A) The appearance of the panel as viewed from above is computed by shooting vertical rays through the panel. By computing the total distances traversed by each ray through each material, the ray-traced images can be obtained. Here three layers each filled with RIG and MPC are shown. Multiple images can be volumetrically encoded in space based on the desired viewing angles. This can be seen in different ray-traced images obtained from a single structure with varying tilting angles. While not explicitly shown here, the volumetric positions of the MPC cells also define the torque in response to a magnetic field. Note that only 3 layers are shown in the schematic for simplicity; in practice, more than 100 layers are typically used. (B) A vertical column of MPC voxels (top) are widened in practice due to droplet spreading (middle) or slight misalignment in the positions of the drops in consecutive layers (bottom).

array and the permanent magnet at which the images should be revealed. The material distribution is generated at the individual cell level as the output, relying on the contrast in the optical and magnetic properties of RIG and MPC. Material assignments for each cell are made at a cell resolution of $3 \times 3 \times 1$ voxels here, i.e. $101.5 \, \mu m \times 101.2 \, \mu m \times 6.4 \, \mu m$.

We represent the material distribution as an indicator function χ_j that describes whether a cell at location j in the panel contains MPC or not. The appearance of a given material distribution and at a given angle is computed by shooting rays from the center of each pixel, tracing

the paths of an array of light rays through the different voxels in the panel (Fig.5A). Here, we assume a diffuse light source illuminating the panels from below and assume that reflection and scattering are negligible. The observer is assumed to be looking at the panel from a sufficiently large distance above the panel. Letting c_{RIG} and c_{MPC} denote the light transmittances of RIG and MPC, the intensity I_k of a pixel k corresponding to a single ray can be written as

$$I_k = c_{RIG}^{d_{RIG}} . c_{MPC}^{d_{MPC}}, \tag{1}$$

where d_{RIG} and d_{MPC} are the total distances traversed by the ray through RIG and MPC respectively. We use measured values of $c_{RIG} \approx 1$ and $c_{MPC} = 0.58$ for the transmittances. The transmittance through 5 layers of MPC, i.e. 3 % of the total thickness of the panels that we optimized in practice, is visually indistinguishable from that of a fully opaque material. Thus, to overcome the limited intensity resolution that can be achieved with MPC, we use half-toning and rely on the ability of the human eye to fuse dotted patterns into continuous tones. We model this by blurring the ray-traced images $I^i(\chi)$ with a 5×5 pixel Gaussian convolution kernel p before comparing them to the input target images. In practice, as shown in Fig. 5B, the dot gain due to droplet spreading or misalignment plays a critical role in the overall appearance. We account for this by correcting the estimated fraction of the materials in each cell prior to ray-tracing by convolving the binary material assignment χ_j with a 3×3 kernel (experimental dot gain measurements and modeling details are in fig. S10 and the Materials and Methods section).

The distribution of the MPC cells inside the panel not only affects its optical properties but also its mechanical behavior under the external magnetic field. Therefore, the two objectives (appearance and angular displacement) are coupled through the locations of the MPC cells. More specifically, each MPC cell contributes to the net torque generated, τ^i, for a given distance d_i (between the panel and the magnet) depending on the position of the cell in the panel.

17

Assuming for now that each lateral ELA hinge connecting the panel to the rigid frame can be modeled as a torsion spring with torsion stiffness κ, the tilting angle assumed by the panel in its equilibrium state can be written as

$$\theta^i = \frac{\tau^i}{2\kappa}. \tag{2}$$

Controlling the torsion bars' stiffness by changing the geometry of the hinges is not sufficient since we want to control various tilting angles simultaneously. Therefore, we fix the dimensions of the hinges and precompute target torques $\tilde{\tau}^i$ to be exerted on the axis of the panel to make it rotate as desired. We then add hard constraints to the optimization that force the torques τ^i corresponding to the distribution χ to match these precomputed torques $\tilde{\tau}^i$. In practice, to account for the nonlinear behavior of the soft ELA hinges, the tilting angle corresponding to a given torque is computed using a finite element method that simulates the deformation of the hinges (soft-joint finite element solver is described in Materials and Methods). The target torques $\tilde{\tau}^i$ are then obtained by using a bisection method. Our original material distribution problem can then be cast as

$$\min_{\chi} E(\chi) = \sum_{i}^{n} \|p * I^i(\chi) - \tilde{I}^i\|_4^4$$
$$\text{s.t. } \tau^i - \tilde{\tau}^i = 0, \forall i \in 1..n, \tag{3}$$

where * denotes the convolution operator. Our use of the L_4 norm is motivated by the fact that, in practice, it offers a good compromise to generate panels with both low average error and low maximum error. Indeed, low index norms help reducing the number of mismatched pixels but might lead to panels for which the maximum error is locally high, which we indeed observed when using a L_2 norm. High index norms help in reducing the magnitude of the maximum error but might lead to a larger number of mismatched pixels. Inspired by stochastic halftoning techniques (*26, 60*), we solve the problem (3) using a simulated annealing (SA) procedure (*61*) augmented with a non-smooth penalty term, which, unlike quadratic penalty functions, allows

for strict satisfaction of the constraints (*62*). For our specific problem we write this additional term as

$$c(\chi) = \sum_i^n \max(0, \|\tau^i(\chi) - \tilde{\tau}^i\|_1 - \epsilon) \qquad (4)$$

and use $\epsilon = 10^{-7}$ MPa to account for small rounding errors when evaluating the torques. The augmented objective $\mathcal{L}$ is then expressed as

$$\mathcal{L}(\chi, T) = E(\chi) + \frac{1}{T}c(\chi), \qquad (5)$$

where T is the simulated annealing temperature. We initialize χ with a 0-valued distribution. At each iteration of the algorithm, a candidate distribution is generated by changing the material assignment of two cells that are randomly selected. We accept the new distribution if it either lowers the objective value or if it raises it with a probability equal to $e^{(\mathcal{L}(\chi_{t-1}, T) - \mathcal{L}(\chi_t, T))/T}$, where $\mathcal{L}(\chi_{t-1}, T)$ and $\mathcal{L}(\chi_t, T)$ are the previous and current objective values and T is the current simulation temperature. This prevents the algorithm from getting trapped in local minima while simultaneously improving the exploration of the entire design space. For our final example, we use 10^8 steps and a linear cooling schedule. Contrary to gradient-based methods commonly used in topology optimization (*15*), our SA procedure does not require a linear system to be solved at every step and can effectively cope with the high number of variables of our problem (one for each of the 10^6 cells). The large number of steps required to approximate a global optimum, typical of SA algorithms, is largely counterbalanced by the fast evaluation of the function (5), which, in practice, can be effectively computed by noting that a change in a voxel material only impacts a few pixels in the ray-traced images.

We applied this methodology for the design and optimization of two different structures, the results of which can be directly fabricated using our printer. The first example consists of a single rotating panel which reveals two different images; one in the rest state and the other at a tilting angle of $30°$ when placed 1.5 cm from the permanent magnet. The im-
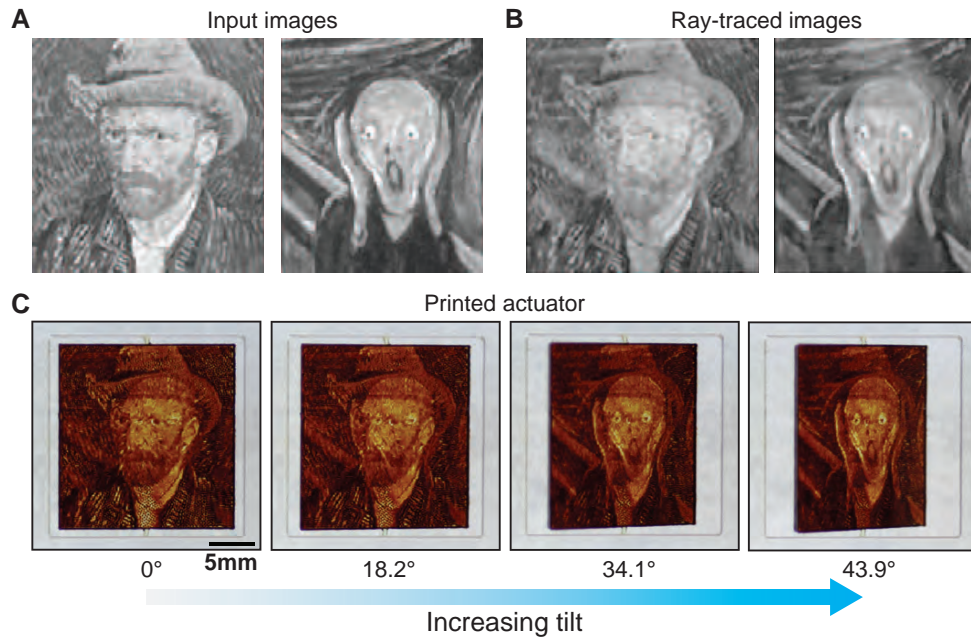
Figure 6: **Panel optimization for both optical and mechanical properties.** Given a pair of target grayscale images **(A)** corresponding to desired top views of the panel array at two different tilting angles (here, 0°and 30°), our topology optimization framework optimizes the distribution of the RIG and MPC in the panels such that they tilt to the desired angles and their appearances match the target images. **(B)** Optimized panel appearances as computed by our ray-tracer. **(C)** Photographs of the 3D-printed topology-optimized sample showing the gradual transition from the "Van Gogh" portrait to the "Scream" image with increasing tilt angle (additional results in fig. S11 and Video S4).

ages correspond to grayscale 186×186 pixel versions of the two paintings *Self-Portrait with Grey Felt Hat* by Van Gogh and *The Scream* by Munch, whose pixel intensities were linearly rescaled to map the range from 0.2 to 0.8. Assignments for the materials are considered at a resolution of 101.5 μm $\times$ 101.2 μm $\times$ 6.4 μm for the panel with external dimensions 18.89 mm $\times$ 18.83 mm $\times$ 1.025 mm (or $186 \times 186 \times 160$ cells). As shown in Fig. 6 and Video S4, the panel rotates as predicted under the applied external magnetic field and displays images that are in good agreement with simulation. The results are shown past the 30° tilt angle; the panel appears narrower in width on tilting. Due to the limit set by the tilting angle, ghosting in areas corresponding to very different intensities in the two target images is visible

in the results of the optimization, and replicated in the prints. This effect is expected and can be reduced by decreasing the dynamic range of the input images a priori.

To evaluate and quantify the performance of the topology-optimized actuator we experimentally measured and simulated the blocking force and the angular deflection as a function of the distance between the actuator and the magnet. We used an offset while positioning the magnet and standardized this in both the experimental setup and in simulations - this is to ensure that the actuator tilts in the same direction consistently given the similarity in the magnetic material content in each half of the actuator. The measurement setup is shown in fig. S12. The blocking force was measured using a calibration cantilever as before (Fig. 3B) as a function of the normal distance separating the magnet and the actuator, and shown in Fig. 7A. The simulation of the identical physical setup was performed in 3D with no fitting parameters and shows a good match with the experimentally obtained forces. The measured angular deflection is shown in Fig. 7B. The variation in the measured and simulated angular deflections are likely due to a mismatch in the printed hinge geometry with respect to the ideal design. A scaled version of the basic design (matching the dimensions of the topology-optimized actuator) was used to perform long-term tests up to 1000 cycles (0.56 Hz) showing no degradation in performance (Fig. 7C, Video S3).

The demonstrated scheme can be easily extended to larger arrays and different images. We demonstrate this with a second example featuring a 3×3 panel array with external dimension $30\ \text{mm} \times 30\ \text{mm} \times 1.025\ \text{mm}$ which is optimized to replicate two textures (grass and stones) at $0°$ and $30°$ respectively (see fig. S11). When the panels are made small, the fraction of MPC required to rotate the panels to the desired angles is significant. This translates into a globally darker area on one half of each panel.
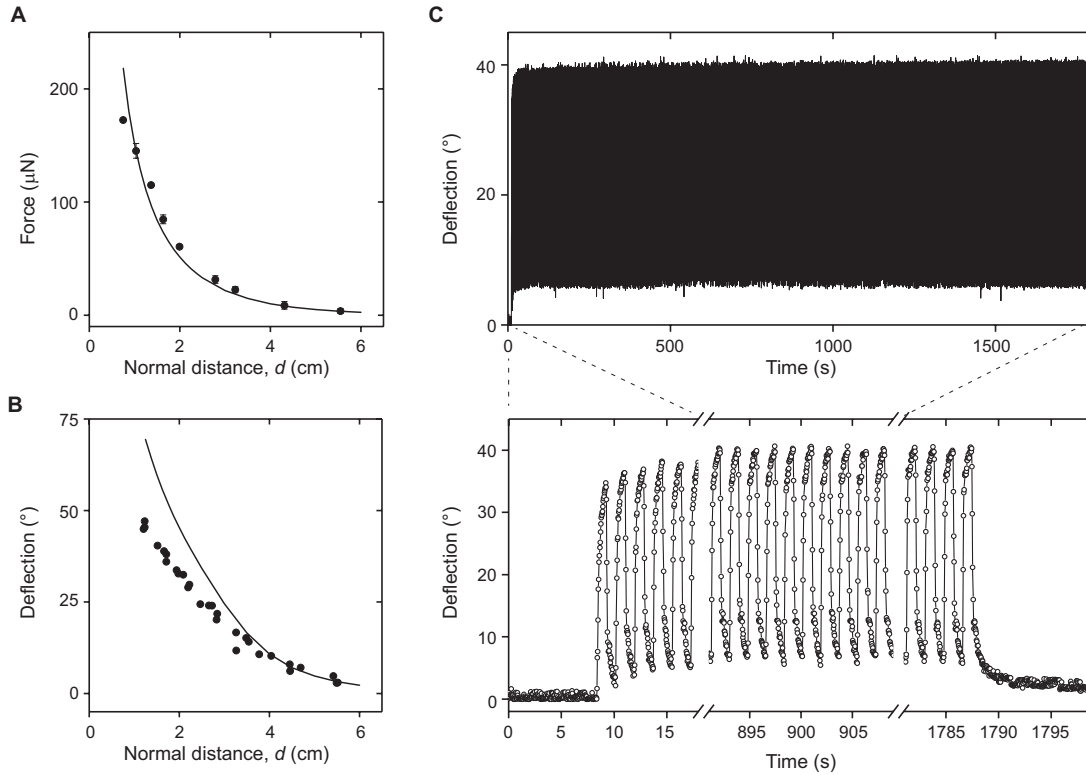
Figure 7: **Characteristics of the topology-optimized actuator and long-term tests. (A)** The blocking force produced by the Van Gogh actuator (Fig. 6) was measured and simulated as function of distance to the magnet. To ensure that the actuator was consistently actuated on the same side each time, the actuating magnet was offset towards one half in all simulations and experimental characterization. The measurement setup is shown in fig. S12. Also note that all simulations are performed without any fitting parameters. **(B)** Measured and simulated angular displacement of the topology-optimized Van Gogh actuator as a function of the normal distance between the actuator and the magnet (setup in fig. S12). **(C)** In order to test the long-term performance of the large actuator and the reliability of the hinges, we cycled a scaled version of the basic design (Fig. 3A) with dimensions identical to the Van Gogh actuator for 1000 cycles (see Video S3).

Discussion

Overall, the actuators shaped by topology optimization demonstrate the ability of our scheme in optimizing complex actuators and its enabling potential in the use of magnetic actuators for camouflage applications. The examples we show here demonstrate two image transitions as

these have the best visual clarity for small actuator thickness (corresponds with printing time). In order to preserve the visual clarity while encoding greater numbers of images (> 2), a larger actuator thickness is required. This is straightforward in our optimization procedure as it is currently written for a flexible number of images. However, this increases the printing time in our fabrication process. Furthermore, in order to improve the optical quality of our printed actuators, we explicitly tailored our droplets to be significantly smaller than the typical droplet size (droplet volume of ~ 8 pL as compared to the typical ~ 22.5 pL). While this flexibility in controlling the process enables the sharp contrast in our images, it comes with the cost of increased printing time. In the future, this speed and size limitation can be overcome by increasing the number of printheads to improve the throughput. Commercial drop-on-demand 3D-printers tackle large scale by utilizing several printheads and offer easy access to this technology, however, they are closed systems that do not allow editing the process or the inks.

The topology optimizer that we developed is aimed at satisfying two different objectives, i.e., matching target optical properties and matching target titling angles. However, in our case, these two objectives are not equally difficult to reach - there are many material distributions that will meet the tilting angle criteria, however it is far more challenging to match the target images exactly. We therefore decided to treat the first goal (target angle) as a hard constraint, and handled the second (target appearance) in the least square sense. However, it is possible to give a more symmetric role to both objectives and therefore generalize the method to problems for which no objective can be exactly met. This would not present any new challenges since we already handle the problem by minimizing a weighted sum. In this sense, the technique that we present could be easily extended to other multi-physics problems, including problems with more than two objectives. This holds as long as fast evaluation of the involved quantities is possible - which demands an efficient problem-specific simulation tool. Another interesting aspect to study when considering multi-physics problems with coupled (and usually conflict-

ing) objectives is related to the Pareto front, i.e., the entire set of optimal trade-offs. How to effectively compute and explore this set in the general case is a fascinating and open research question.

Drop-on-demand inkjet-based 3D-printing is well suited in the fabrication of topology-optimized designs and in generating high-resolution optical properties due to its ability to print with a large number of nozzles at high resolution and with multiple inks at once. However, the printing process demands inks within very tight rheological properties and particle sizes - this makes it challenging to develop diverse functional inks (*57*). Increasing the actuating force (and in parallel, reducing the power requirements) can be easily achieved by improving the loading of the magnetic nanoparticles in the ink. We observed that our MPC ink was unstable when the loading of Fe_3O_4 nanoparticles was increased above 12 wt%. The use of anisotropically shaped magnetic nanoparticles resulted in frequent clogging of the nozzles. Despite the remaining challenges in developing new inks and materials a wide range of materials can be currently fabricated using this process: UV curable rigid and stretchable acrylate polymers, liquid electrolytes, conductive and semiconducting films (*36*). Using similar printing processes, other groups have demonstrated a wide range of different actuators including electrically-actuated dielectric elastomer actuators (*55, 56*).

The MPC ink we use here allows tuning the optical properties and the force generated by a voxel simultaneously. In that sense, magnetic materials and actuation are particularly useful here along with their ability to be controlled without physical tethers. However, it is still challenging to actuate a large array of actuators in close proximity that are each individually controllable. Generating magnetic fields with well-controlled spatially varying intensities is a long-standing challenge. This is not a problem we address here but it is useful to note that this is an important requirement for individually addressable arrays in the future. Recent progress on achieving selective control of magnetic elements have relied on spatial field control (*63, 64*)

24

as well as selective actuation using aligned nanoparticles (*65*).

Fully designing the entire pipeline - starting inks, device architectures, optimization-based design synthesis and printing hardware - enhances our freedom in controlling each of these individual elements. It also allows us to account for the physical system in our optimization, i.e., our optimization is fabrication aware. For instance, we take into account the effects of droplet spreading while evaluating the optical appearance properties. Likewise, the loading of the Fe_3O_4 nanoparticles in the MPC ink results in increased opacity of the ink but the use of half-toning allows us to expand on the range of perceived pixel intensities. However, it is useful to note that fabrication-aware optimization is closely tied to the specific set of materials and fabrication processes used - any changes to the materials or fabrication process would require reevaluation of these physical effects. Furthermore, the ability to control each of these parameters increases the overall complexity of our pipeline.

The topology-optimized actuator presented here is an example of a coupled multifunctional system with more than 10^6 design dimensions. The accompanying fabrication toolkit can be used to design actuators along with sensors and basic computing elements such as transistors and amplifiers (*42*). In order to enable the vision of robotic/autonomous composites that unify materials and machines (*1, 2, 42*) an integration of a multitude of functions is required. There remain challenges in developing different specific elements (sensors, processors and actuators) as well as broader challenges in their subsequent large-scale integration and enabling overall self-sufficiency (by integrating power sources and communication elements). These developments are expected to be accompanied by increases in the complexity of materials, design demands, and fabrication processes, but also in the complexity of the overall system architecture. Much of these foundational strategies are yet to be developed. We expect that the automated design and fabrication of optimized, multifunctional actuators with minimal human intervention is a step towards tackling this broader challenge.

25

Conclusion

We demonstrate an approach that unifies multimaterial 3D-printing with topology optimization and brings us one step closer to automated fabrication from purely functional goals. The topology optimization procedure generates complex high-dimensional designs while optimizing multiple objectives while our printing process enables the direct fabrication of these topology-optimized, multimaterial designs. We specifically demonstrate this by optimizing and fabricating a multimaterial actuator that displays two independent images at specific deflection angles, controlled by an applied magnetic field. Voxel-level flexibility in material choices from both the fabrication and shape optimization perspective enables the first steps towards fully-automated design and fabrication of complex, multimaterial devices.

Materials and Methods

3D-printing process summary

We use a custom built inkjet based 3D-printer that takes a voxel-based structure as input for printing as previously reported (*42, 54*). All the inks used in this work are made from acrylate based monomers and oligomers that can be crosslinked by UV light initiated free radical polymerization. The UV LED array in our printer used in this work has an intensity ~ 2.1 W/cm^2 at 365 nm. The thin elastic (ELA) hinges used in our actuator designs are fragile. To facilitate easy removal, our samples were printed on a 125 μm sheet of polyimide(PI) (McMaster-Carr, Elmhurst, IL, USA) coated with a thin layer of poly(acrylic acid) (PAA ~ 50 kg/mol, ~ 25 % sol. in water, Polysciences Inc., USA), prepared by drop casting. On completion of the print (typical print time $\sim 2 - 3$ h), the samples on the PAA-coated polyimide substrates were left in water overnight by which time, the printed part is detached from the substrate. For our samples with a silver mirror finish (Fig. 4B & 4C), the silver layer was prepared by drop casting a reac-

tive silver ink on a PI substrate and then sintered at 80 °C for 2 mins on a hotplate. Structures printed on top of the silver ink can be easily detached from the PI substrate since the precipitated silver nanoparticles adhere strongly to our UV cured polymers and weakly with the PI substrate. We used a 1:1 (vol) mixture of H_2O_2:NH_4OH as the silver etchant to remove freely exposed silver.

Elastic and rigid acrylate polymer inks

The rigid polymer (RIG) ink was formulated by mixing the following components: 59 wt% of Genomer1117 (Rahn USA Corp., (5-ethyl-1,3-dioxan-5-yl) methyl acrylate), 32 wt% of Genomer 2252/G (Rahn USA Corp., vinyl ester resin/epoxy acrylate) and 9 wt% of M300 (Rahn USA Corp., trimethylolpropane-triacrylate). The components were mixed together and stirred at 600 rpm at room temperature for 1 h. 2 wt% of Irgacure819 (BASF Chemical Company, bis(2,4,6-trimethylbenzoyl)-phenylphosphineoxide) was added as the photoinitiator for free radical polymerization under UV-light. 0.1 wt% of 4-methoxyphenol (Sigma Aldrich Corp.) was added to inhibit free radical polymerization for any trace amounts of free radicals induced by ambient light or impurities, and improve the resolution.

The elastic (ELA) ink was formulated by mixing 48 wt% of CN3105 (Sartomer USA LLC., low viscosity oligomer), 33 wt% of SR504 (Sartomer USA LLC., ethoxylated (4) nonyl phenol acrylate), 5 wt% of Genomer4215 (Rahn USA Corp., aliphatic polyester urethane acrylate) and 10 wt% SR313B (Sartomer USA LLC., C12 C14 alkyl methacrylate). The mixture was heated at 60 °C for 1 h, and then stirred at 600 rpm for 1 h. 1 wt% of Irgacure819 and 0.5 wt% of ITX (Rahn USA Corp., isopropylthioxanthone) were added as photoinitiators. 0.1 wt% of 4-methoxyphenol was added to inhibit free radical polymerization. All inks were stored in UV-protected containers to inhibit curing from ambient light.

Colored inks were prepared with pigment dispersions (RJA dispersions LLC) added to the

rigid ink formulation. The magenta and cyan pigmented inks were prepared by adding 1g of the dispersion to 100 g of the rigid ink formulation. The white pigmented ink was prepared by adding 5 g of the pigment dispersion to 100 g of the rigid ink formulation. All inks were then stirred at 600 rpm for 1 h and then filtered with a 1 micron filter before use.

Ink viscosities were measured using a viscometer (DV-I Prime, Brookfield Engineering) and optimized to be $\sim 11 - 15$ cP at 70°C. Surface tension of the inks were measured using a tensiometer (DCAT11, Dataphysics) and optimized to be $\sim 30 - 35$ mN/m at the print conditions.

Magnetic nanoparticle - polymer (MPC) composite ink

The magnetic nanoparticle-based ink was formulated as follows: 12 wt% of Iron(III)-Oxide nano-particles (US Research Nanomaterials Inc.), 80 wt% of the rigid ink formulation (without photoinitiators and photoinhibitors), and 8 wt% of Genomer1116 were mixed together. 5 wt% of DISPERBYK110 (BYK Additives & Instruments, nonionic dispersant) was added on top of the total weight of the iron(III)oxide mixture (5 g of dispersant added for every 100 g of magnetic ink). The magnetic ink was then run on a bead-mill (M100 VSE TEFC, Engineered Mills, Inc., USA) with 300 μm yttria-stabilized zirconia beads for 7 h at 4000 rpm to break down agglomeration and stabilize the nano-particles within the suspension. After milling was completed, the ink was transferred to a clean 250 mL container. 2 wt% of Irgacure819 and ITX was added to the suspension and mixed vigorously with a spatula for several minutes. 0.1 wt% of 4-methoxyphenol was added finally as a photo-polymerization inhibitor. The ink was allowed to sit for 6 h to completely dissolve the photoinitiators in the ink. The ink was then filtered with a 1 μm filter before use.

Polymer characterization measurements

Thermogravimetric analysis (TGA) measurements were performed using a Discovery-TGA (TA Instruments, USA). A 3D-printed slab of magnetic material (1 mm x 1 mm x 0.5 mm) was placed on top of a platinum pan and the sample temperature was ramped from 50 °C to 800 °C in air at a 10 °C/min ramp rate. The retained weight percent of the MPC was measured to 11.93% verifying the nanoparticle loading (fig. S1A). A larger weight percentage was measured when TGA was performed in nitrogen-rich atmosphere - potentially resulting from excess polymer retention after the tests.

Vibrating Sample Magnetometry (VSM) measurements

VSM measurements were performed using an 800-VSM model (Microsense, USA). 8 mm disks of the MPC material were 3D-printed with varying thicknesses (0.1 mm to 1 mm), mounted on glass tips and characterized. Typically the applied magnetic field was cycled between -10^4 Oe to 10^4 Oe. The magnetization of the MPC samples saturated to ~ 5.7 emu/g.

Mechanical characterization

The stress-strain curve for each material was measured on a table top mechanical tester Instron 5944 (Instron, Norwood, MA, USA) with a 2 kN max load. The samples were 3D-printed and mechanically tested. The rigid polymer and MPC material were measured at 0.5 mm/min strain rate, and the elastic polymer was measured at 1.5 mm/min. The measured modulus for RIG, ELA, and MPC are 1290 MPa, 528 kPa, and 507 MPa respectively (see main text). Poisson's ratio measurements were performed on 3D-printed samples of the elastic material using designs with 4 circular features along the x and y axis of the sample. These axis aligned point pairs are positioned at equal distances. Samples were clamped on the Instron mechanical tester and a set of images were taken at various controlled strains. The distance along the x and y- axis along the

4 circular points were measured at varying strains with the optical microscope imaging software (Stream start software, Olympus Corp., Tokyo, Japan). Fig. S1B shows these measurements. The Poisson's ratio was measured to be ~ 0.4.

Spectrophotometer measurements

Transmission spectra were measured in the optical wavelength using a color i5 bench-top spectrophotometer (X-Rite, USA). A square slab at varying thicknesses (ranging from 40 to 110 µm) was 3D-printed and the transmittances of the samples were measured (see main text).

Actuator characterization: force, deflection and bandwidth measurements

The actuator characteristics in Fig. 3 were recorded by optical tracking of deflections. For the measurements of forces, a cantilever cut from 0.002" thick polyimide sheet was used. The rectangular cantilever was laser cut with dimensions 0.6" in length and 0.125" in width. The stiffness of the cantilever at the tip was established to be 105.9 ± 12.0 mN/m by applying different loads. To measure the blocking force, the calibrated cantilever tip was placed at the actuator edge with the largest displacement and the displacement was measured using optical images. The force was calculated from the displacement and the stiffness of the calibrated cantilever. The angular deflections were directly measured from the optical images. The actuator force and deflection measurement were performed using the 2" $\times$ 2" $\times$ 0.5" magnet to generate the magnetic field. To measure the angular displacement with time for the bandwidth measurements, the edges of cantilever were tracked from the side (for the small-amplitude displacements) and from the top (for the large-amplitude bandwidth) for each frame. Here the electromagnet was used for actuation, powered by 1.5 A at 50% duty cycle (for small-amplitude) and 7.5 A at 50% duty cycle (for large-amplitude bandwidth measurements). For the 7.5 A current pulses, a solid-state relay (SSR-25 DD) was controlled by a source meter. All these images and videos

were acquired using the Canon macro lens (EF 180 mm f/3.5L Macro USM).

Dot gain - measurements and simulation details

Dot gain measurements were performed by 3D-printing two striped-pattern prints (2 voxel wide and 4 voxel wide stripes) of the MPC and the rigid polymer ink. Dot gain was computed by measuring the actual width with respect to the expected design width. Samples were imaged using an optical microscope SZ61 (Olympus Corp. Tokyo, Japan) fitted with the SC30 digital camera (Olympus Corp. Tokyo, Japan). The widths of the stripes of both prints were measured using imaging the Stream start software (Olympus Corp., Japan). The width of the MPC traces and the rigid ink of the 2-voxel wide stripes were ~ 90 μm and ~ 50 μm respectively. The corresponding widths for the 4-voxel wide stripes were ~ 180 μm and ~ 100 μm respectively (fig. S10). The dot gain of the droplets are typically symmetric in the in-plane directions.

So in practice, a column of voxels containing MPC appears, on average, 30 μm wider than the width of the original droplets deposited by the printer. Dot gain is typically due to drop spreading and slight misalignment in the positions of the drops of consecutive layers. To account for these effects, we correct the estimated fraction, or presence probability, of magnetic ink in each voxel prior to ray-tracing the light. This is performed layer by layer by convolving the original binary material distribution with a 3×3 kernel q of the form

$$q = \frac{u}{\|u\|} \frac{v^T}{\|v\|}, \ u^T = [s_x r_x s_x], \ v^T = [s_y r_y s_y], \tag{6}$$

where $s_i = 15$μm, for $i = x, y$, is the measured lateral spread of the drops in the in-plane directions and r_x and r_y are the voxel resolution along x and y respectively. The filtered material ratios are used to scale the individual distance contributions of voxels in the calculation of the total distances d_{RIG} and d_{MPC} traversed by the rays.

Soft-joint simulation

Each joint connecting the panels to the frame is modeled as a hexahedral lattice with 16^3 elements and simulated with a finite element method using linear basis functions and 8 quadrature points per element. For the ELA material, we use a Neo Hookean material model with energy density $W = \frac{\mu}{2}(I_1 - 3 - 2\ln(J)) + \frac{\lambda}{2}(\ln(J))^2$, where I_1 and J are respectively the first invariant of the right Cauchy-Green deformation tensor and the determinant of the deformation gradient and λ and μ are the Lamé parameters. In order to account for any fabrication related effects, we further estimate the effective elastic modulus of the ELA hinge (357.7 kPa) independently from fabricated calibration actuators in fig. S2. The measured Young's modulus (E) and Poisson's ratio (ν) can be converted to Lamé parameters λ and μ using $\lambda = E\nu/((1+\nu)(1-2\nu))$ and $\mu = E/(2(1+\nu))$. The panels and the frame are treated as rigid bodies. The forces acting on the panels are computed on a voxelized representation of the panel geometry. We consider both gravitational forces acting on all the voxels of the panels, and magnetic forces due to the external magnetic field acting on the MPC cells. Each of these voxels is modeled as a magnetic dipole with moment $\mathbf{m}_i$ located at the center $\mathbf{c}_i$ of the voxel and aligned with the external magnetic field. The force $\mathbf{F}_i$ acting on the magnetized voxel is thus described by $\mathbf{F}_i = \nabla(\mathbf{m}_i.\mathbf{B})$. We model the magnetization of the MPC cell using the hyperbolic tangent function as $M(\mathbf{H}) = \pm 5.67 \tanh(2.8 \times 10^{-2}\sqrt{\|H\|_2})$, with $\mathbf{H}$ expressed in $[Oe]$, which is in good agreement with the measured data (fig. S13D). The magnitude m_i of the moment $\mathbf{m}_i$ is then approximated by $m_i(\mathbf{c}_i) = M(\mathbf{H}(\mathbf{c}_i))\rho_{MPC}dV$, where $\rho_{MPC} =\sim 1.2$ g/cm^3 denotes the density of the cured MPC material and dV corresponds to the volume of an individual voxel. Note that the moment generated by a MPC cell is not constant but depends on the current location of the voxel center which is affected by the rotation of the panel.

Magnetic field - experimental setup, field computation and measurements

For our variable magnetic field experiments, we constructed an electromagnet using a consumer grade microwave oven transformer. The transformer was cut to enforce a flux path outside the core, and the secondary coil was removed. The primary coil (~ 114 turns) is retained in the core to generate the magnetic field. In laser rastering experiments (Fig. 4B, main text), the primary coil was connected to a current source (up to 7.5 A). This allowed the field to be dynamically controlled up to ~ 45 mT at the sample location. The steepest gradient in the magnetic field is normal to the plane of the 6 mirror array causing the mirrors to tilt out of plane.

For our remaining experiments, we used a $2" \times 2" \times 0.5"$ bar-shaped Neodymium grade N52 magnet magnetized along its vertical axis (y) to generate the external magnetic field. In all our static deflection measurements, we placed the samples ~ 1 cm from the surface of the magnet, along the magnetic axis. In this case, the magnetic field can be derived analytically from the Maxwell equations (*66*) and is a function of the dimensions a, b, c, of the magnet (fig. S13A) and its magnetization $\mathbf{M} = M\mathbf{e}_z$ that we assume to be constant. Letting the origin of the coordinate system be located at the center of the magnet, the field $\mathbf{H} = (H_x, H_y, H_z)$ can be written as

$$H_x(x,y,z) = \frac{M}{4\pi} \sum_{k,l,m=1}^{2} (-1)^{k+l+m} \ln(y + (-1)^l b + r_{klm}(x,y,z)), \tag{7}$$

$$H_y(x,y,z) = \frac{M}{4\pi} \sum_{k,l,m=1}^{2} (-1)^{k+l+m} \ln(x + (-1)^k a + r_{klm}(x,y,z)), \tag{8}$$

$$H_z(x,y,z) = \frac{M}{4\pi} \sum_{k,l,m=1}^{2} (-1)^{k+l+m} \mathrm{atan}\left(\frac{(x + (-1)^k a)(y + (-1)^l b)}{(z + (-1)^m c)r_{klm}(x,y,z)}\right), \tag{9}$$

$$r_{klm}(x,y,z) = \sqrt{(x + (-1)^k a)^2 + (y + (-1)^l b)^2 + (z + (-1)^m c)^2}. \tag{10}$$

We used $M = 950$ kA/m as the value for the magnetization, obtained by fitting the analytical magnetic flux density $\mathbf{B} = \mu_0 \mathbf{H}$ to sample values (see fig. S13B & 13C).

All our magnetic field measurements were performed using a F. W. Bell 9500 gauss meter with a probe (~ 4.5 mm$\times 4.5$ mm). Measurement were typically made in the 3 kG range, which has a reported accuracy of ± 30 G (or the 300 mT range, ± 3 mT).

Silicone oil-water interface experiments

Interfacial tension measurements were performed with the DataPhysics FDS tensiometer (DataPhysics, Germany) using the PT11 Wilhelmy plate (10 mm $\times$ 19.9 mm $\times$ 0.2 mm) for air-fluid interface and with the RG11 Du Nouy Ring (18.7 mm diameter, 0.37 mm wire thickness) for the silicone oil-water interface.

Imaging and processing

All images and videos were acquired using DSLR camera (Canon EOS 60D, or Canon EOS-1D-X, Canon, USA). White balance and exposure were adjusted for visual clarity. Canon macro lens (EF 180 mm f/3.5L Macro USM), Canon Zoom EFS 18-55 mm f/3.5 - 5.6, and Canon Zoom EF 28-80 mm f/3.5 - 5.6 were the lenses used.

Supplementary Materials

Fig. S1. Material characteristics

Fig. S2. Experimental verification of tilting angles

Fig. S3. 2-axis tilting panels

Fig. S4. Dynamic Mechanical Analysis (DMA) of elastic hinge material family

Fig. S5. Large-amplitude bandwidth measurements

Fig. S6. Long-term cycling

Fig. S7. Experimental setup for dynamic actuation

Fig. S8. 3D-printed water lily design

Fig. S9. Spike actuator arrays design

References

1. M. A. McEvoy, N. Correll, Materials that couple sensing, actuation, computation, and communication. *Science* **347**, 1261689 (2015).

2. Y. Mengüç, N. Correll, R. Kramer, J. Paik, Will robots be bodies with brains or brains with bodies? *Science Robotics* **2**, eaar4527 (2017).

3. R. Hanlon, C.-C. Chiao, L. Mäthger, A. Barbosa, K. Buresch, C. Chubb, Cephalopod dynamic camouflage: bridging the continuum between background matching and disruptive coloration. *Philosophical Transactions of the Royal Society of London B: Biological Sciences* **364**, 429–437 (2009).

4. L. F. Deravi, A. P. Magyar, S. P. Sheehy, G. R. Bell, L. M. Mäthger, S. L. Senft, T. J. Wardill, W. S. Lane, A. M. Kuzirian, R. T. Hanlon, *et al.*, The structure–function relationships of a natural nanoscale photonic device in cuttlefish chromatophores. *Journal of The Royal Society Interface* **11**, 20130942 (2014).

5. D. Panetta, K. Buresch, R. T. Hanlon, Dynamic masquerade with morphing three-dimensional skin in cuttlefish. *Biology letters* **13**, 20170070 (2017).

6. L. J. Hornbeck, 128×128 deformable mirror device. *IEEE Transactions on Electron Devices* **30**, 539–545 (1983).

7. C. Gong, T. Hogan, Cmos compatible fabrication processes for the digital micromirror device. *IEEE Journal of the Electron Devices Society* **2**, 27–32 (2014).

8. P. Vettiger, G. Cross, M. Despont, U. Drechsler, U. Durig, B. Gotsmann, W. Haberle, M. Lantz, H. Rothuizen, R. Stutz, *et al.*, The" millipede"-nanotechnology entering data storage. *IEEE Transactions on nanotechnology* **99**, 39–55 (2002).

9. L. Wen, J. C. Weaver, P. J. Thornycroft, G. V. Lauder, Hydrodynamic function of biomimetic shark skin: effect of denticle pattern and spacing. *Bioinspiration & Biomimetics* **10**, 066010 (2015).

10. A. W. Lang, M. T. Bradshaw, J. A. Smith, J. N. Wheelus, P. J. Motta, M. L. Habegger, R. E. Hueter, Movable shark scales act as a passive dynamic micro-roughness to control flow separation. *Bioinspiration & biomimetics* **9**, 036017 (2014).

11. S. L. Tamm, Mechanical synchronization of ciliary beating within comb plates of ctenophores. *Journal of experimental biology* **113**, 401–408 (1984).

12. B. Anderson, J. Shultz, B. Jayne, Axial kinematics and muscle activity during terrestrial locomotion of the centipede scolopendra heros. *Journal of experimental biology* **198**, 1185–1195 (1995).

13. H. Cruse, What mechanisms coordinate leg movement in walking arthropods? *Trends in neurosciences* **13**, 15–21 (1990).

14. H. Cruse, V. Dürr, J. Schmitz, Insect walking is based on a decentralized architecture revealing a simple and robust controller. *Philosophical Transactions of the Royal Society of London A: Mathematical, Physical and Engineering Sciences* **365**, 221–250 (2007).

15. M. P. Bendsøe, O. Sigmund, *Topology Optimization: Theory, Methods and Applications* (Springer-Verlag Berlin Heidelberg, 2003).

16. M. P. Bendsøe, N. Kikuchi, Generating optimal topologies in structural design using a homogenization method. *Comput. Methods Appl. Mech. Eng.* **71**, 197–224 (1988).

17. J. S. Jensen, O. Sigmund, Systematic design of photonic crystal structures using topology optimization: Low-loss waveguide bends. *Applied Physics Letters* **84**, 2022-2024 (2004).

18. O. Sigmund, On the design of compliant mechanisms using topology optimization. *Mechanics of Structures and Machines* **25**, 493-524 (1997).

19. H. Zhang, M. Y. Wang, F. Chen, Y. Wang, A. S. Kumar, J. Y. H. Fuh, Design and development of a soft gripper with topology optimization. *2017 IEEE/RSJ International Conference on Intelligent Robots and Systems (IROS)* pp. 6239–6244 (2017).

20. K. Maute, A. Tkachuk, J. Wu, H. Jerry Qi, Z. Ding, M. L. Dunn, Level set topology optimization of printed active composites. *Journal of Mechanical Design* **137** (2015).

21. C. Schumacher, B. Bickel, J. Rys, S. Marschner, C. Daraio, M. Gross, Microstructures to control elasticity in 3d printing. *ACM Trans. Graph.* **34**, 136:1–136:13 (2015).

22. J. D. Hiller, H. Lipson, Automatic design and manufacture of soft robots. *IEEE Transactions on Robotics* **28**, 457-466 (2012).

23. N. Cheney, R. MacCurdy, J. Clune, H. Lipson, Unshackling evolution: evolving soft robots with multiple materials and a powerful generative encoding. *ACM SIGEVOlution* **7**, 11–23 (2014).

24. K. Shea, J. Cagan, S. Fenves, A shape annealing approach to optimal truss design with dynamic grouping of members. *ASME Journal of Mechanical Design* **119** (1997).

25. K. Shea, J. Cagan, Innovative dome design: Applying geodesic patterns with shape annealing. *Artificial Intelligence for Engineering Design, Analysis and Manufacturing* **11**, 379394 (1997).

26. A. Bermano, I. Baran, M. Alexa, W. Matusik, SHADOWPIX: Multiple Images from Self Shadowing. *Computer Graphics Forum* (2012).

27. S. A. Morin, R. F. Shepherd, S. W. Kwok, A. A. Stokes, A. Nemiroski, G. M. Whitesides, Camouflage and display for soft machines. *Science* **337**, 828–832 (2012).

28. C. Larson, B. Peele, S. Li, S. Robinson, M. Totaro, L. Beccai, B. Mazzolai, R. Shepherd, Highly stretchable electroluminescent skin for optical signaling and tactile sensing. *Science* **351**, 1071–1074 (2016).

29. J. Pikul, S. Li, H. Bai, R. Hanlon, I. Cohen, R. Shepherd, Stretchable surfaces with programmable 3d texture morphing for synthetic camouflaging skins. *Science* **358**, 210–214 (2017).

30. B. H. Cumpston, S. P. Ananthavel, S. Barlow, D. L. Dyer, J. E. Ehrlich, L. L. Erskine, A. A. Heikal, S. M. Kuebler, I.-Y. S. Lee, D. McCord-Maughon, *et al.*, Two-photon polymerization initiators for three-dimensional optical data storage and microfabrication. *Nature* **398**, 51–54 (1999).

31. J. A. Lewis, Direct ink writing of 3d functional materials. *Advanced Functional Materials* **16**, 2193–2204 (2006).

32. T. Xu, W. Zhao, J.-M. Zhu, M. Z. Albanna, J. J. Yoo, A. Atala, Complex heterogeneous tissue constructs containing multiple cell types prepared by inkjet printing technology. *Biomaterials* **34**, 130–139 (2013).

33. M. S. Mannoor, Z. Jiang, T. James, Y. L. Kong, K. A. Malatesta, W. O. Soboyejo, N. Verma, D. H. Gracias, M. C. McAlpine, 3d printed bionic ears. *Nano letters* **13**, 2634–2639 (2013).

34. S. Babaee, J. Shim, J. C. Weaver, E. R. Chen, N. Patel, K. Bertoldi, 3d soft metamaterials with negative poisson's ratio. *Advanced Materials* **25**, 5044–5049 (2013).

35. Q. Ge, C. K. Dunn, H. J. Qi, M. L. Dunn, Active origami by 4d printing. *Smart Materials and Structures* **23**, 094007 (2014).

36. S. Sundaram, D. S. Kim, M. A. Baldo, R. C. Hayward, W. Matusik, 3d-printed self-folding electronics. *ACS applied materials & interfaces* **9**, 32290–32298 (2017).

37. A. Curodeau, E. Sachs, S. Caldarise, Design and fabrication of cast orthopedic implants with freeform surface textures from 3-d printed ceramic shell. *Journal of Biomedical Materials Research Part A* **53**, 525–535 (2000).

38. C. Ladd, J.-H. So, J. Muth, M. D. Dickey, 3d printing of free standing liquid metal microstructures. *Advanced Materials* **25**, 5081–5085 (2013).

39. K. Sun, T.-S. Wei, B. Y. Ahn, J. Y. Seo, S. J. Dillon, J. A. Lewis, 3d printing of interdigitated li-ion microbattery architectures. *Advanced Materials* **25**, 4539–4543 (2013).

40. D. Kokkinis, M. Schaffner, A. R. Studart, Multimaterial magnetically assisted 3d printing of composite materials. *Nature communications* **6** (2015).

41. J. J. Martin, B. E. Fiore, R. M. Erb, Designing bioinspired composite reinforcement architectures via 3d magnetic printing. *Nature communications* **6** (2015).

42. S. Sundaram, Z. Jiang, P. Sitthi-Amorn, D. S. Kim, M. A. Baldo, W. Matusik, 3d-printed autonomous sensory composites. *Advanced Materials Technologies* (2017).

43. A. Ghosh, P. Fischer, Controlled propulsion of artificial magnetic nanostructured propellers. *Nano letters* **9**, 2243–2245 (2009).

44. C. L. Van Oosten, C. W. Bastiaansen, D. J. Broer, Printed artificial cilia from liquid-crystal network actuators modularly driven by light. *Nature materials* **8**, 677–682 (2009).

45. J. V. Timonen, C. Johans, K. Kontturi, A. Walther, O. Ikkala, R. H. Ras, A facile template-free approach to magnetodriven, multifunctional artificial cilia. *ACS applied materials & interfaces* **2**, 2226–2230 (2010).

46. T.-Y. Huang, M. S. Sakar, A. Mao, A. J. Petruska, F. Qiu, X.-B. Chen, S. Kennedy, D. Mooney, B. J. Nelson, 3d printed microtransporters: compound micromachines for spatiotemporally controlled delivery of therapeutic agents. *Advanced Materials* **27**, 6644–6650 (2015).

47. L. Hines, K. Petersen, G. Z. Lum, M. Sitti, Soft actuators for small-scale robotics. *Advanced Materials* **29** (2017).

48. J. Kim, S. E. Chung, S.-E. Choi, H. Lee, J. Kim, S. Kwon, Programming magnetic anisotropy in polymeric microactuators. *Nature materials* **10**, 747–752 (2011).

49. Y. Zhu, D. S. Antao, R. Xiao, E. N. Wang, Real-time manipulation with magnetically tunable structures. *Advanced Materials* **26**, 6442–6446 (2014).

50. R. M. Erb, J. J. Martin, R. Soheilian, C. Pan, J. R. Barber, Actuating soft matter with magnetic torque. *Advanced Functional Materials* **26**, 3859–3880 (2016).

51. O. Cugat, J. Delamare, G. Reyne, Magnetic micro-actuators and systems (magmas). *IEEE Transactions on magnetics* **39**, 3607–3612 (2003).

52. W. Hu, G. Z. Lum, M. Mastrangeli, M. Sitti, Small-scale soft-bodied robot with multimodal locomotion. *Nature* **554**, 81 (2018).

53. H. Lipson, J. B. Pollack, Automatic design and manufacture of robotic lifeforms. *Nature* **406**, 974 (2000).

54. P. Sitthi-Amorn, J. E. Ramos, Y. Wangy, J. Kwan, J. Lan, W. Wang, W. Matusik, Multifab: a machine vision assisted platform for multi-material 3d printing. *ACM Transactions on Graphics (TOG)* **34**, 129 (2015).

55. C. Baechler, S. Gardin, H. Abuhimd, G. Kovacs, Inkjet printed multiwall carbon nanotube electrodes for dielectric elastomer actuators. *Smart Materials and Structures* **25**, 055009 (2016).

56. D. McCoul, S. Rosset, S. Schlatter, H. Shea, Inkjet 3d printing of uv and thermal cure silicone elastomers for dielectric elastomer actuators. *Smart Materials and Structures* **26**, 125022 (2017).

57. B. Derby, Inkjet printing of functional and structural materials: fluid property requirements, feature stability, and resolution. *Annual Review of Materials Research* **40**, 395–414 (2010).

58. S. Y. Chin, Y. C. Poh, A.-C. Kohler, J. T. Compton, L. L. Hsu, K. M. Lau, S. Kim, B. W. Lee, F. Y. Lee, S. K. Sia, Additive manufacturing of hydrogel-based materials for next-generation implantable medical devices. *Science Robotics* **2**, eaah6451 (2017).

59. G. Wetzstein, D. Lanman, M. Hirsch, R. Raskar, Tensor displays: compressive light field synthesis using multilayer displays with directional backlighting. *ACM Transactions on Graphics (TOG)* **31**, 80 (2012).

60. W.-M. Pang, Y. Qu, T.-T. Wong, D. Cohen-Or, P.-A. Heng, Structure-aware halftoning. *ACM Transactions on Graphics (TOG)* **27**, 89:1–89:8 (2008).

61. S. Kirkpatrick, C. D. Gelatt, M. P. Vecchi, Optimization by simulated annealing. *Science* **220**, 671–680 (1983).

62. J. Nocedal, S. J. Wright, *Numerical Optimization* (Springer, 2000).

63. E. Diller, J. Giltinan, M. Sitti, Independent control of multiple magnetic microrobots in three dimensions. *The International Journal of Robotics Research* **32**, 614–631 (2013).

64. J. Rahmer, C. Stehning, B. Gleich, Spatially selective remote magnetic actuation of identical helical micromachines. *Science Robotics* **2**, eaal2845 (2017).

65. S. R. Mishra, M. D. Dickey, O. D. Velev, J. B. Tracy, Selective and directional actuation of elastomer films using chained magnetic nanoparticles. *Nanoscale* **8**, 1309–1313 (2016).

66. M. McCaig, *Permanent Magnets in Theory and Practice* (Wiley, 1977).